KERNFORSCHUNGSANLAGE JÜLICH GmbH
Institut für Reaktorwerkstoffe

Thermal Shock Testing of Ceramics with Pulsed Laser Irradiation

by

Robert Benz
Aristides Naoumidis
Hubertus Nickel

Jül - 2056
April 1986
ISSN 0366-0885

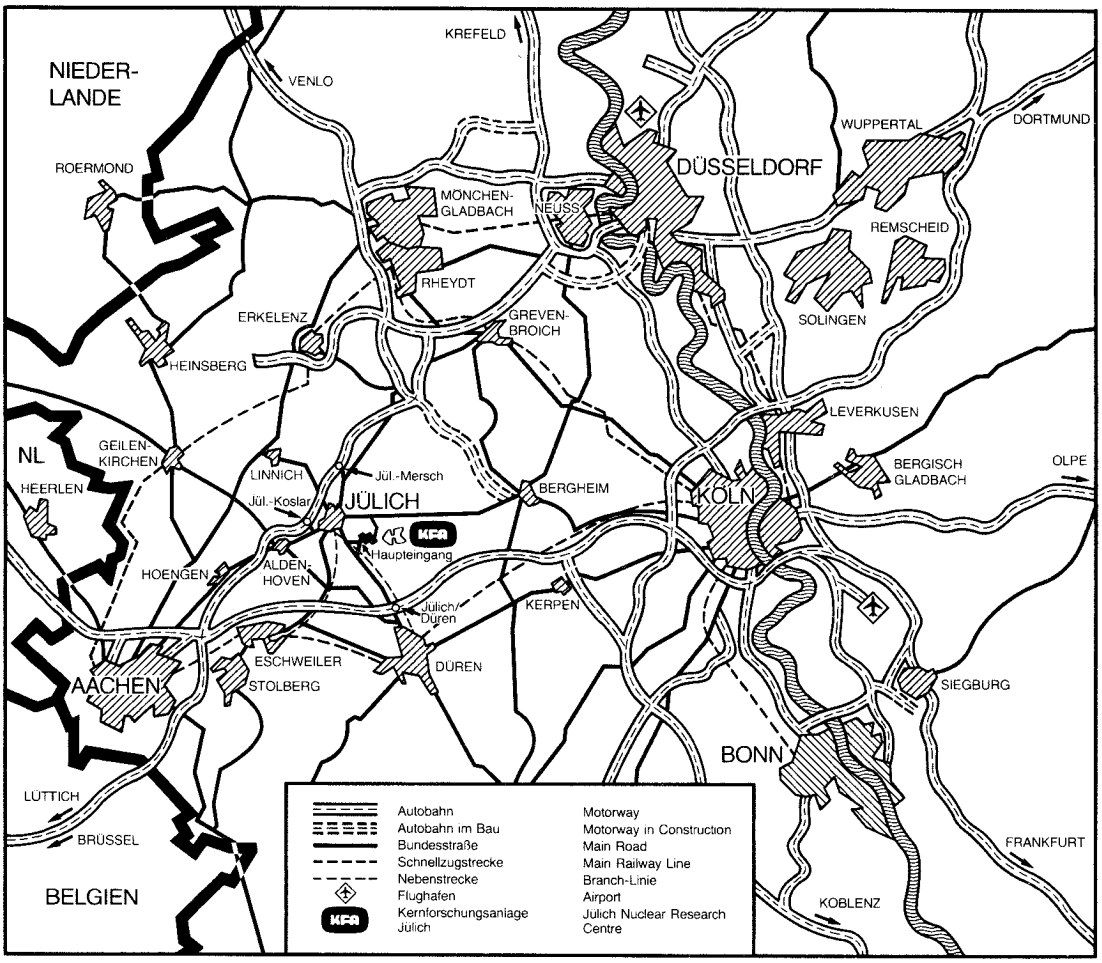

Als Manuskript gedruckt

Berichte der Kernforschungsanlage Jülich – Nr. 2056

Institut für Reaktorwerkstoffe Jül - 2056

Zu beziehen durch: ZENTRALBIBLIOTHEK der Kernforschungsanlage Jülich GmbH
Postfach 1913 · D-5170 Jülich (Bundesrepublik Deutschland)
Telefon: 02461/610 · Telex: 833556-0 kf d

Thermal Shock Testing of Ceramics with Pulsed Laser Irradiation

by

Robert Benz
Aristides Naoumidis
Hubertus Nickel

Kernforschungs-
anlage Jülich
GmbH IRW

Jül-2056

April 1986

Thermal Shock Testing of Ceramics with Pulsed Laser Irradiation

by

R. Benz
A. Naoumidis
H. Nickel

ABSTRACT

Arguements are presented showing that the resistance to thermal stressing ("thermal shock") under pulsed thermal energy deposition by various kinds of beam irradiations is approximately proportional to $\Phi_a\sqrt{t_p}$, where Φ_a is the absorbed power density and t_p is the pulse length, under conditions of diffusivity controlled spreading of heat. In practical beam irradiation testing, incident power density, Φ, is reported. To evaluated the usefulness of $\Phi\sqrt{t_p}$ as an approximation to $\Phi_a\sqrt{t_p}$, damage threshold values are reviewed for different kinds of beams (electron, proton, and laser) for a range of t_p values 5×10^{-6} to 2s.

Ruby laser beam irradiation tests were made on the following ceramics: AlN, BN, graphite, α-SiC, β-SiC coated graphites, $(\alpha+\beta)Si_3N_4$, CVD (chemical vapor deposition) TiC coated graphite, CVD TiC coated Mo, and CVD TiN coated IN 625. The laser beam pulse lengths investigated were 9×10^{-4} (normal) and 5×10^{-6}s (saturable dye Q-switched) and the power densities ranged from 25 to 4000 kW/cm^2 corresponding to $\Phi\sqrt{t_p}$ values of 0.8 to 8.8 kJ/cm^{2}s$^{1/2}$.

The identified failure mechanisms are:

1) plastic flow followed by tensile and bend fracturing,
2) chemical decomposition,
3) melting, and
4) loss by thermal spallation.

The materials most resistant to thermal spallation and having thermal threshold $\Phi\sqrt{tp}$ values of 0.8 $kJ/cm^2s^{1/2}$ or higher are pyrolytic graphite, POCO AXF-5Q graphite, β-SiC coated graphites, CVD TiC coated graphite, and CVD TiC coated Mo. The hot-pressed polycrystalline AlN, BN, and Si_3N_4, α-SiC and CVD TiN coated IN 625 are most susceptible to thermal spallation and, in some cases, show thermal stress cracking and chemical decomposition at $\Phi\sqrt{tp}$ = 0.8 $kJ/cm^2s^{1/2}$. The specimens of β SiC coated graphite show good resistance to spalling loss up to $\Phi\sqrt{tp}$ = 1.6 $kJ/cm^2s^{1/2}$, however, both the β SiC coatings and the technical grade α-SiC may undergo substantial chemical decomposition under the more extreme conditions.

In view of the theoretical approximations and the neglect of reflection losses there is reasonable accord between the damage threshold $\Phi\sqrt{tp}$ values from the laser, electron, and proton beam tests.

CONTENTS

List of Tables

List of Figures

Fig. 6: SEM micrograph of AlN after being irradiated with one normal pulse at 3 mm defocus: $\Phi\sqrt{tp} = 1.6$ kJ/cm^{2}s$^{1/2}$.
The rim of an erosion crater is seen. Thermostress cracks and condensed Al globules (product of AlN thermal decomposition) are present.

Fig. 7: SEM micrograph of pyrolytic graphite viewed parallel to the layer planes running vertically after pulsing for 5 times with normal laser radiation at 2 mm defocus: $\Phi\sqrt{tp} = 4.8$ kJ/cm^{2}s$^{1/2}$.
Thermal stress splitting of the layer planes in the test area (upper central part of the picture) is seen. Surface restructuring with periodicities of ~ 10 µm is seen. This is much coarser than the restructuring feature sizes of 0.2 µm seen in layer planes irradiated normally (cf. Fig. 6 of Sone et al.[60]).

Fig. 8: SEM micrograph of CVD TiC-coated AXF-5Q graphite after Q-switch laser pulsing for 5 times at 2 mm defocus: $\Phi\sqrt{tp} = 0.8$ kJ/cm^{2}s$^{1/2}$.
Melting of TiC followed by intergranular thermal-stress fracturing during cool down is seen. The fracture patterns is the same as that observed with massive TiC grown by diffusion reaction and subjected to the same test. This shows that the cracking is an inherent characteristic of TiC and not derived from differential thermal expansion between the coating and substrate.

Fig. 9: SEM micrograph of CVD TiC coated AXF-5Q graphite after Q-switch laser pulsing for 30 times at 6 mm defocus: $\Phi\sqrt{tp} = 0.56$ kJ/cm^{2}s$^{1/2}$.
Thermal stress cracking and evidence of fusion is seen. Outer layers of some of the coating have peeled away from the underlying TiC. Nakamura et al.[49] have previously reported a similar tendency to delaminate in CVD TiC coatings under H^+ bombardment with $\Phi\sqrt{tp} = 1.5$ kJ/cm^{2}s$^{1/2}$.

Fig. 10: SEM micrograph of CVD TiC coated Mo after normal laser pulsing for 5 times at 3 mm defocus: $\Phi\sqrt{tp} = 1.6$ kJ/cm^{2}s$^{1/2}$.
Partial melting and intergranular cracking is apparent. TiC lowers the melting point of Mo due to eutectic formation[25].

1. INTRODUCTION

Materials for the 1st wall and limiters in nuclear fusion devices must be able to withstand depositions of extremely high power densities estimated at 0.3 to 15 kW/cm^2 mainly as particle bombardment[65]. Limiters are designed to receive the greatest thermal loadings and the material candidates are refractories most of which are brittle. Minimum plasma temperatures required for ignition of the fusion reactions have been estimated at 10^8 to 10^9 K corresponding to the hydrogen-isotope energy of 10 to 100 keV and to penetration ranges in relevant materials of about 1 to 150 µm (within a factor of 2), respectively[60]. The energies of the ions and electrons from the plasma impinging on the limiter will be deposited in surface layers of this thickness and generate corresponding temperature gradients as high as 10^9 to 10^7 K/m. The depositions will fluctuate in time being resolvable into a) slow oscillations (1-s periods) from burn pulsing and b) superimposed transients with a wide spectrums of uncontrolled, often shorter, periods, e.g. arcing and runaway electrons[25,67]. Under the proposed operating conditions, limiters in a nuclear fusion device with energy returns will be subjected to extreme temperatures and to severe temperature gradients. Such temperature gradients can generate thermal stresses and strains that may well be decisive in curtailing the limiter's useful life.

As an aid in selection of wall materials, thermal shock and thermal fatigue tests have been made on a number of materials. In the past, electron and proton beams have been used almost exclusively to simulate the thermal energy deposition. Use of electron beams has the advantage among other things that the electron penetration depth and its dependence on impact energy and the target Z is very similar to that of protons, a major plasma ion component, being 1 to 150 µm for 10 to 100 kV electrons.

Other techniques for deposition of high power densities are available. Laser irradiation is a relatively economical technique for producing pulsed power and energy densities of practically unlimited intensities. This work was undertaken to investigate the ruby laser beam as a method for thermal shock testing of selected ceramic materials. Some characteristics of the laser beam are compared with those of the electron beam in Table 1.

Table 1: Comparison of the ruby laser and electron beam interaction with solids

	Photons	Electrons (and similar for protons)
Particle energy	1.8 ev (max. 9 ev by up to 5 multi-photon processes)	5 to 150 keV
Energy coupling	target electron system	mainly the target electron system
Energy dose distribution	Exponential absorption $I_0(1-R)\mu e^{-\mu z}$, where μ (absorption coefficient), R (reflectivity), I_0(incident power density),	Semitruncated Gaussian, stopping power $\simeq$ Z/E lnJ, where Z (atomic number), E (electron energy), J (mean ionization potential)[9]
Penetration depth	Generally dependent on wave length. Values for opaque materials range from 10^{-8}m in metals to 10^{-6}m in seminconductors[68].	Typical electron ranges are 1.5μm for 10 keV to 150μm for 150 keV in graphite and Si and lower in higher Z materials[61].
Energy loss mechanisms	Reflection (sensitive to beam power density being rapidly supressed by self induction at $I_0 > 10^7$ W/cm^2)[53]. Photo- and thermionic emission.	Back reflection of primary and secondary electrons varies from 5-40 % depending on energy and target Z, Bremsstrahlung is important only at higher energies.
Peculiarities	Self induction enhanced absorption at high power densities.	Space charge accumulation on insulators.
Pulse lengths that are here cited.	9×10^{-4} and 5×10^{-6} s.	0.1 to 10 s.
Thermalization times	$\sim 10^{-9}$s.	$\sim 10^{-8}$ s.

2. THEORETICAL

2.1 Energy deposition by laser beam irradiation

The range of photons in an absorbing mediums depends on the photon energy, $E = h \cdot \nu$, the beam intensity, and the target free-carrier density. When ordinary visible radiation enters a homogeneous absorbing medium by normal incidence on a plane surface, its intensity is reduced as function of the penetration depth, z, in accordance with the equation

$$I(W/cm^2) = I_0(1-R)e^{-\mu z} \qquad (1)$$

where $I_0(W/cm^2)$ is the incident intensity assumed to have a uniform spacial distribution over a finite surface area perpendicular to the direction of propagation, R is the surface reflectivity, and μ^{-1} is the extinction depth (inverse of the absorption coefficient, μ). The corresponding dose distributions is

$$\frac{dI}{dz}\ (W/cm^3) = -I_0(1-R)\mu e^{-\mu z} \qquad (2)$$

Photons are absorbed by a mechanism of electron excitation and it is useful to consider the order of magnitudes of the relaxation times of the processes involved. The photon-electron excitation times are less than 10^{-12}s [12,26,32,73]. The electron-phonon relaxation times are less than 10^{-9}s [5,72]. Thus, the net photon-phonon thermalization times are less than 10^{-9}s [5,37,41,71] and ca. 10^{-8}s [42]. The latter value is much less than the ruby laser pulse lengths employed in this work, viz. 5 µs and 0.9 ms. Thus, the radiation can be regarded as being absorbed practically instantaneously as thermal energy with the same spacial distribution as the absorbed photon dose distribution given above in Equation (2). The thermal energy is deposited with an exponental distribution and any spreading by free carriers (or electron-hole plasma) is negligible. With the ruby laser wave length, λ = 693 nm, typical extinction depths, μ^{-1}, range from 0.014 µm for the good electronic conductor Cu, to the order of 1 µm for the semi-conductor Si, to higher values for insulators and optically transparent materials. These figures have to be qualified somewhat, however, because laser beams can be of such high intensity as to cause opaque targets to become heated.

The reflectivity of metal surfaces generally decrease with increasing temperature and at sufficiently high temperatures specular surfaces become roughtened causing an increased absorptivity[3]. Additionally, at extremely high power densities of $> 10^8 W/cm^2$, these and other self induction effects are found to occur that still are not well understood[1,2,6,10,13,17,52,53]. The net result is that absorption of laser radiation is usually much greater than the ordinary optical reflectivity and absorption data would indicate.

Initially, when the laser beam first impinges on the target, thermal stresses are induced the intensity of which are governed by the thermal energy dose distribution much as that of an electron beam is governed by the electron range. There is an important difference, however, in that it is not practical to adjust the extinction depth of the laser beam as the range of the electrons can be adjusted by varying the electron energy. After the initial burst, the thermal stresses will be determined by the rate at which the heat spreads by conduction. In the present experiments (the subsequently discussed Case III), the thermal diffusion lengths, $\sqrt{4D_T t_p}$*, in relevant materials under normal and Q switch radiation with the pulse lengths 9×10^{-4} and 5×10^{-6}s, respectively, range from 4 to 220 μm and are generally greater than the extinction depths estimated at 0.1 to 1 μm, cf. Columns 7 and 8 of Table 2. Similarly, the thermal diffusion lengths in the subsequently cited particle beam tests with pulse lengths of 0.1 to 2 s are at least 0.66 to 5 mm for the various materials and are much greater than the particle ranges of 1 to 150 μm, Column 6 of Table 2. Thus, both the laser and the electron and proton beam tests are physically similar in that the thermal stresses at the temperature peak (end of the pulse) are both governed by the deposited heat distribution as it spreads by conduction. In what follows, arguements leading to an approximate relation of the test parameters, power density, pulse length, and to the target thermal stress resistance are outlined.

---

* where $D_T(cm^2/s) = \lambda / \rho \cdot C_V$ is the thermal diffusivity of the target material assumed to be homogeneous, λ (W/cm-K) is the heat conductivity, $\rho \cdot C_V$ is the heat capacity per cm^3, and t_p is the radiation pulse length.

Table 2: Representative values of some physical properties for some high temperature ceramics α (linear average expansion coefficient), E (Young's modulus), D_T (thermal diffusivity), and calculated $\sqrt{4D_T t_p}$ (thermal diffusion depths) values.

Material	Density (Th. value) g/cm^3	α x10^6 K^{-1}	E, GN/m^2	D_T, cm^2/s	$\sqrt{4D_T t_p}$, mm			References
					t_p=0.1s	t_p=0.9ms	t_p=5µs	
AlN	3.21(3.26)	6.5	216-336	0.05	1.4	0.13	0.011	58)
Al_2O_3	3.9(3.965)	7.6	320-390	0.012	0.69	0.066	0.0049	19,33,58,20)
B_4C		4.8						
BN	2.08(2.25)	5.8	110	0.047	1.4	0.13	0.010	58)
Graphite	1.8(2.26)	7.7	3.5-77	0.13	2.3	0.22	0.016	59,23)
Pyrolytic graphite								
1.c direction	1.8-2.2	28.0	17	0.00305	0.35	0.033	0.0025	19)
2.a direction		0.95		0.635	5.0	0.48	0.036	
α-SiC	3.217	4.4	210	0.024	1.0	0.093	0.0069	33,50)
SiC+Si		4.4	300					
β SiC	(3.217)	4.5	427	0.056	1.5	0.14	0.011	51)
Si_3N_4(HP)	2.45-3.2 (3.44)	2.1-2.7	90-290	0.011	0.66	0.063	0.0047	28,30,33,40) 43,50)
Si_3N_4(RB)	2.7-2.9							
TiC	(4.93)	7.7	320-450	0.101	2.0	0.19	0.014	50)
TiN	(5.22)		200	0.052	1.4	0.14	0.010	50,33)
ZrO_2(partially stabilized)	5.75	6.5	200	0.0044	0.42	0.040	0.0030	14)
Ni	8.90	16.0	200	0.19	2.4	0.26	0.019	59,64)
Mo	10.2	6.5	325	0.26	3.2	0.31	0.023	59,64)
W	19.35	5.4	411	0.34	3.7	0.012	0.026	59,64)

2.2 One dimensional heat transfer approximation

Specimens 1 cm thick plate-shaped were employed and the diameter of the impinging laser beam was generally greater than the thermal diffusion depths, $\sqrt{4D_T t_p}$. The heat transfer during the pulse is approximated as a one-dimensional problem with the partial differential equation

$$\frac{\partial^2 T}{\partial z^2} - \frac{1}{D_T}\frac{\partial T}{\partial t} = -\frac{I_0(1-R)\mu}{\lambda} e^{-\mu z} \qquad (3)$$

subject to the conditions 1) that the initial temperature is uniform, formulated by letting the temperature rise be everywhere 0,

$$\Delta T(z,0) = 0, \quad z \geq 0, \quad t = 0 \qquad (3a)$$

and 2) that the material region is semi-infinite,

$$\lim_{z \to \infty} \Delta T(z,t) = 0, \quad t \geq 0 \qquad (3b)$$

In Equations (3), the positive direction of the spacial coordinate z is oriented inwards from the material surface and t denotes time. The general solution to this heat problem is given by Carslaw and Jaeger[15] from which the particular integral is

$$\boxed{\Delta T(z,t) = \frac{I_0(1-R)}{\lambda}\left[\sqrt{4D_T t}\ \text{ierfc}\left(\xi\right) - \frac{e^{-\mu z}}{\mu}\right],} \qquad (4)$$

where $\xi = z/\sqrt{4D_T t}$, $\text{ierfc}(\xi) = \int_{\xi}^{\infty} \text{erfc}(u)\, du$ and

$$\text{erfc}(u) = (1-\text{erf}(u)) = \frac{2}{\sqrt{\pi}} \int_{y}^{\infty} e^{-y^2}.\, dy.$$

In application of this equation for different tests four different regimes are distinguished depending on the pulse length, t_p.

Case I. $t_p < (\mu^{-1} v_s) \approx 10^{-9}$s, where v_s is the pressure or stress shock speed, ca. 2000 to 5000 m/s. The propagation depth of the thermal stress wave is, in this case, less than the optical extinction depth. With the extremely short pulse lengths of less than 1 ns, pressure stress waves are created[69] that are superimposed upon and interfere with the identification of thermal shocks[16,29]. Also during this period, thermal stressing may be sensitive to the kinetics of thermalization of the beam energy and inertial effects may become significant[75]. Extremely short pulses can lead to secondary stress effects that complicate the thermal stresses and are to be avoided.

Case II. $10^{-7} > t_p > 10^{-9}$s. Under these conditions, the optical extinction depth is greater than the thermal diffusion depth, $\mu^{-1} > \sqrt{4D_T t_p}$, just as in the Case I. They differ from those of Case I in that the power density and the intensity of the induced stress waves are assumed to cause negligible direct mechanical stressing. The thermal diffusion is negligible and the temperature distribution is controlled by the distribution of deposited energy

$$\frac{1}{D_T} \frac{d}{dt} \Delta T = \frac{I_0(1-R) \cdot \mu e^{-\mu z}}{\lambda} \tag{5}$$

from which the surface temperature rise is calculated as

$$\Delta T(0,t) = \frac{I_0(1-R) \cdot \mu t}{\rho \cdot C_v}, \quad (0 < t \leq t_p) \tag{6}$$

the time rate of surface temperature change as

$$\Delta T(0,t) = \frac{I_0(1-R) \cdot \mu}{\rho \cdot C_v}, \quad (0 < t \leq t_p) \tag{7}$$

and the surface temperature negative gradient as

$$-\frac{d}{dz} \Delta T(0,t) = \frac{I_0(1-R) \cdot \mu^2 T}{\rho \cdot C_v} = \mu \cdot \Delta T(0,t), \quad (0 < t \leq t_p) \tag{8}.$$

Ruby and Nd lasers with Pockel cells for Q switching are commercially available that give the prescribed pulse lengths. It appears that such pulse lengths may give a better fundamental understanding of thermal shock than those of the following described, thermal diffusion controlled thermal shockes (Case III). Because

1. rates of temperature change are higher by a factor of 10^3 and the temperature gradients are higher by 10^6,
2. massive thermal diffusion and interference by melting can be reduced.

Case III. 1 s tp 10^{-6}s. The optical extinction depth is much less than the thermal diffusion depth, $\mu^{-1} \ll \sqrt{4D_T t_p}$. The surface temperature rise under these conditions is calculated from Equation (4) neglecting re-radiation effects as

$$\Delta T(0,t) = \frac{2I_0(1-R)\ t}{\rho \cdot C_V \sqrt{\pi\ D_T}} \quad (t < t_p) \tag{9}.$$

The rate of change the surface temperature is

$$\frac{d}{dt} \Delta\ T(0,t) = \frac{I_0(1-R)}{\rho \cdot C_V \sqrt{\pi \cdot D_T t}} \quad (t < t_p) \tag{10}.$$

The surface temperature gradient is

$$\lim_{z \to 0} \frac{d}{dz} \Delta T(z,t) = 0 \tag{11}.$$

and heat transfer by the thermal diffusion mechanism prevails.

These equations describe a first approximation to the conditions under which the subsequently described tests were made with normal and Q-switched ruby lasers. According to these equations the surface temperature is proportional to $t^{1/2}$ and the rate of change of the surface temperature is proportional to $t^{-1/2}$. Mass and Vernickel[45] have discussed how to refine the calculation of the surface temperature under the present pulse heating conditions by taking into account the following effects which were neglected above:

1. heat loss by re-radiation and
2. temperature dependences of the thermophysical properties λ and $\rho \cdot C_V$.

Case IV. $t_p > 3s$. The steady state condition, $\frac{d^2}{dz^2}\Delta T = 0$. Under these conditions the specimen dimensions, ca. 10 mm, plays a role in determining thermal strains. The thermal expansion induced compressive thermal stresses during heat up extend to depths comparable to that of the counteracting tensile stresses on the opposite, cooler, side. This generates bending moments across the entire specimen and, depending on the specimen size and the relative tensile and compressive strengths, irreversible ductile or brittle failure may occur. Such failures can be expected when relatively large areas are irradiated for long periods of over 3 s. Such failure is not to be expected with laser beam tests having tiny localized areas of heating and relative short heating periods except with materials with very low tensile-to-compressive strength ratios.

The Equations (3) to (11) were derived under the assumptions of one-dimensional heat flow in a homogeneous medium with temperature independent material properties. These conditions apply only for sufficiently short irradiation periods and sufficiently low absorb power densities, $I_0(1-R)$, that no phase change takes place. The course of the surface temperature and surface temperature gradients at $t > t_p$ are not described. Keeping these limitations in mind it can be concluded that with increasing time the surface temperature will initally increase in proportion to t (up to ca. 10^{-7}s) and eventually as $t^{1/2}$ in the time region 10^{-6} to 1 s. At the same time the surface temperature negative gradient will initially scale as t, go through a maximum, and tend to 0. Thus, it would appear that, in order to induce thermal shock failure during the heat up phase, the shortest pulse length should be used that is compatible without incurring side effects such as pressure stress wave shocking.

2.3 Thermal stress geometry

Thermal stresses arise when thermal expansion within a solid is nonuniform. Two fundamentally different kinds of thermal stresses are, σ_1, which is due to differences in composition or anisotropy in a polycrystalline body and may arise even in uniformly heated bodies and, σ_2, due exclusively to temperature differences or gradients within the body. Stresses add vectorily and a material subjected to only σ_2 will perform with a greater apparent strength than that with the same temperature distribution but subjected to

$\sigma_1 + \sigma_2$ thermal stresses. Thus, in design of materials to have thermal shock resistance, generally, σ_1 should be minimized. The following discussion pertains to only the σ_2-type thermal stresses.

The test geometry in the subsequently described experiments were in all cases the same. Plate specimens with 10-mm thicknesses, large compared to the thermal diffusion depth, $\sqrt{4D_T t_p}$, were irradiated with a ruby laser beam having a diameter large compared to $\sqrt{4D_T t_p}$. To emphasize the physics involved, the simplifying assumption is made that the heat-dose-distribution affected zone at the initial instant of irradiation is a surface flat zylinder as depicted in Fig. 1a. With advance in time the heat spreads much as indicated with the solid lines.

Thermal stresses arising from the above described temperature distributions are idealized as illustrated in Fig. 1b. The rim of the heated disc is assumed to be clamped to the surrounding colder region of the body but free to expand in the direction normal to the surface. Three different kinds of thermal stresses are indicated under heat up, 1. in-plane radial compression, 2. surface normal shear at the disc rim, and 3. a bending moment which evolves from the shear stress at the heat spreads with passage of time. A surface tangential shear at the disc rim is not illustrated. At sufficiently low test power densities, the target material will behave elastically and experience a transverse compressive stress distribution during heat up represented by the equation for an isotropic body[63,38,34,48]

$$\sigma(z,t) = \frac{E \cdot \alpha \cdot \Delta T(z,t)}{(1-\nu)} \tag{12}$$

where E is the Young's modulus, α is the linear thermal expansion coefficient, ν is the Poisson's ratio, and $\Delta T = T - T_0$ is the surface temperature change relative to the initial stress free state.

An equation of similar form applies for the normal stresses and bend moments. The thermal stresses are represented symbolically by the simple general form

$$\sigma = S \frac{E \cdot \alpha \cdot \Delta T}{(1-\nu)} \tag{13}$$

where S is a geometrical factor.

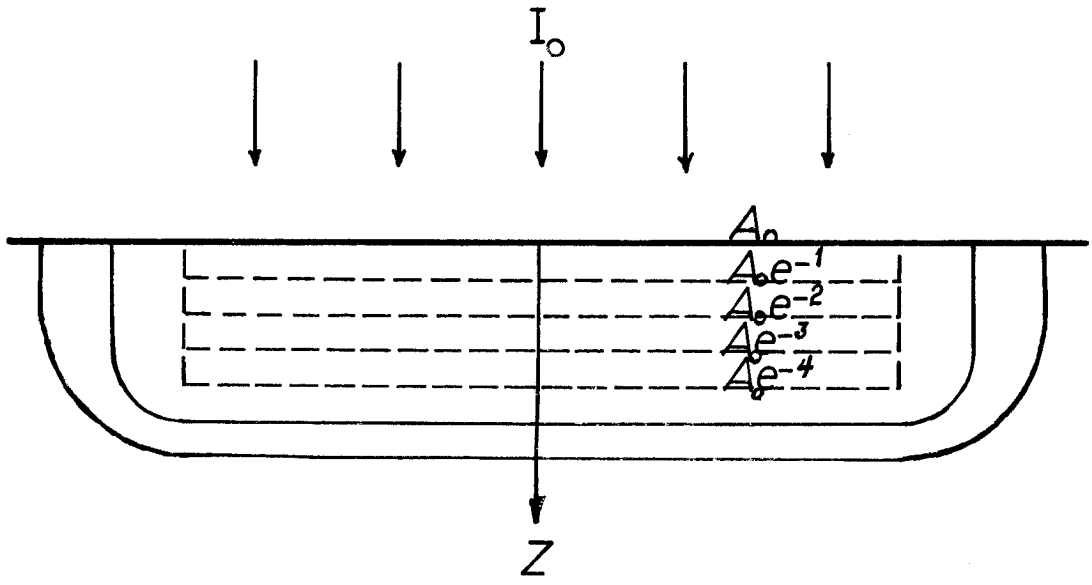

Fig. 1a: Cross section of the disc-shaped surface test region showing schematically surfaces of constant energy dose (broken lines). Two isotherms at the end of a finite heat pulse length that results from spreading of heat conduction are shown qualitatively as solid lines $A_o = I_o(1-R)\mu$.

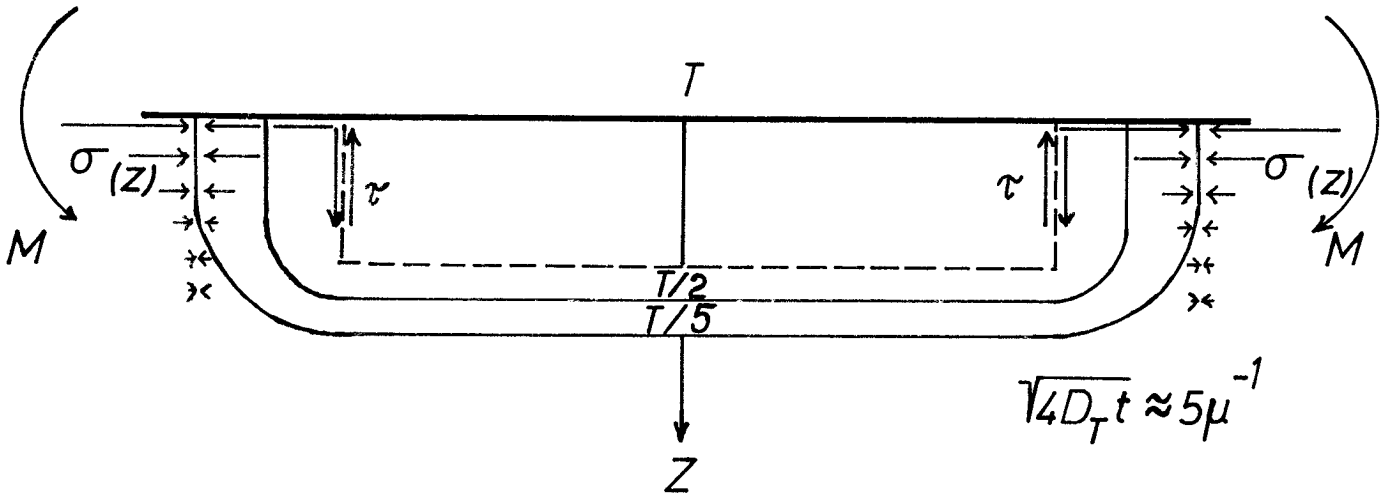

Fig. 1b: Cross section of the surface test region showing schematically the thermal stress distribution corresponding to the temperature distribution illustrated in Fig. 1a. Three kinds of stresses are indicated,

1. Plane radial compressive stresses on the heat disc, σ,

and an initial

2. shear stress at the edge of the heated disc parallel to the z axis, τ,

which changes with spreading of the thermal energy into

3. a complex of bending moments, M.

A tangential component perpendicular to the secional view is not represented.

In principle, if all the material physical and mechanical properties and their temperature dependence is known, it should be possible to calculate the time evolution of reversible thermal stresses given the local space and temporal variation of temperature[20]. Such data are not available.

2.4 Thermal stress failure mechanism

Elastic failure will occur when the temperature differences are sufficiently strong that the thermal stress exceeds some critical fracture strength, σ_c, or yield stress, σ_γ.

Neglecting any temperature variation of the relevant physical properties, thermal stress failure will occur when the surface temperature in the described test geometry just exceeds the minimum critical value

$$\Delta T_c = S \frac{\sigma_c(1-\nu)}{\alpha \cdot E}, \tag{14}$$

where σ_c is the critical stress associated with a specified failure mode. The quantity $\sigma_c(1-\nu)/\alpha \cdot E$ is called a thermal stress resistance parameter[18]. Each mode of failure will be induced by its peculiar critical gradient or temperature and can be characterized by its corresponding threshold value, ΔT_c. Relative ΔT_c values can serve as a basis of comparison of the performance of different materials under thermal shock stressing[22] with fixed geometry.

Transient surface temperatures as implied in ΔT_c are difficult to measure reproducibly and ΔT_c is not a convenient observable. The laser average power density, $I_0(1-R)$, regarded as being distributed over a surface layer of thickness $\sqrt{4D_T t_p}$ is, however, related to a mean temperature by the energy balance equation

$$I_0(1-R)t_p = \rho \cdot C_v \cdot \Delta T \sqrt{4D_T t_p} \tag{15}$$

from which

$$\Delta T = B I_0 \sqrt{t_p} \tag{16},$$

where $B = (1-R)/2\sqrt{\lambda \cdot \rho \cdot C_v}$ is a constant characteristic of the material and the radiation.

The subsequent discussion is generalized to all the discussed kinds of radiation and particle beams and the corresponding generalized incident flux density is denoted by Φ(kW/cm^2) in place of I_0. The thermal stress failure threshold value $(\Phi\sqrt{t_p})_c$ characterizes the intensity of the thermal loading which causes thermal stresses and eventually thermal damage and is a practicable measure of ΔT_c because both Φ and t_p are conveniently evaluatable. The threshold temperature for thermal stress yielding in surfaces of metals subjected to pulsed irradiation has been previously suggested to have the same form as Equation (16)[48].

In the above formulation, Equation (16) does not contain local temperature gradients but only the overall temperature change. It may, therefore, be expected that $\Phi\sqrt{t_p}$ will, also, be useful for characterizing thresholds for thermally activated damage mechanisms such as chemical decomposition, melting, and vaporization as already suggested by Behrisch[8] and reviewed by McCracken and Stott[44]. For each failure mechanism, i, the proportionality constant, Bi, in the equation

$$(\Phi\sqrt{t_p})_i = \Delta T_{c,i}/B_i \qquad (17)$$

will, of course, contain a different group of physical quantities. In testing practice, it is not the absorbed, but, rather, the incident power density that is measured. Any difference in energy loss by reflection between tests is either estimated or ignored. It is part of the present task of comparing available $\Phi\sqrt{t_p}$ values to see to what extent this approximation is useful. The critical thermal load values $(\Phi\sqrt{t_p})_c$ for a given failure mechanism should be the same regardless of the manner by which the thermal energy is deposited (whether by laser, electron or proton beams) so long as the temperature distribution at the end of the pulse t_p is diffusivity controlled. This may not be true in the case of the effects from knock-on atoms created by electrons or sputtering induced by protons that begin at particle energies of ca. 120 keV or for other higher energy processes.

Surface inhomogeneities can lead to thermal stress failures in ways not embranced in the above described model. Surface asperities and surface texture, e.g. roughness, pores, microcracks, grain boundaries, absorbed gases or nonuniform chemical compositions, can lead to nonuniform deposition of ener-

gy in surface layers and to microcrystalline fragmentation. As the tiny crystallites spall off, the underlying freshly formed surface becomes exposed to a sudden change in radiation intensity imposing a renewed sudden change in the surface temperature gradients and to thermal stresses. The spalling process then repeats itself. This kind of thermal stress failure is very probably exacerbated by high-pressure streaming of outgassing and by pressure shock waves known to occur when materials are pulse irradiated. Surface material lost in this manner will not be distinguished from that lost by other mechanisms such as vaporization and chemical decomposition. All such losses are lumped together in the subsequent discussion under the term "thermal spallation". The term "thermal spallation" appears to have been introduced by Kingery[38].

Many parameters can influence the ability of a material to survive thermal stressing under pulsed beam irradiation. Use of the product $\tilde{\Phi}\sqrt{t_p}$ is suggested for ranking and characterizing thermal stress damage thresholds in different kinds of beams over a wide range of pulse lengths.

3. EXPERIMENTAL

Thermal pulse irradiation tests were made with 6-mm diameter and 100-mm long ruby crystals in cavities energized by a Xenon flash lamps. One laser was operated in the normal, free-running manner. The length of the pulse envelope was 0.9 ms. The average energy spacial distribution approximated a Gaussian (slightly elliptic). The second laser was Q-switched with the saturable dye solution consisting of vanadium phthalocyanine in nitrobenzene having a concentration adjusted to give a single pulse. The pulse was saw-tooth shaped with a rise time of ca. 5 ns and a width at half maximum of 5 µs. The average energy spacial density was Gaussian. The average energy outputs were measured with a carbon calorimeter as 0.38 ± 0.02 J for the normal and 0.052 ± 0.005 J for the Q-switched laser. Power density of the laser beam emergent from a 23-mm focal length convex lens and normally incident on the specimen surface was adjusted by defocussing.

The materials tested together with some of their properties are listed in Table 3. Except for the pyrolytic graphite specimen with layer planes parallel to the surface which received no pretreatment, surfaces of the 10-mm

Table 3: Thermal stress tested ceramic materials

Material	Description	Manufacturer	Lattice spacings, pm a_o	c_o	Pore vol.,%	Density g/cm^3	Coating thickness µm
1. AlN	hot pressed	ESK Kempten	310.9±0.3	497.7±1.0	15		
2. AlN	hot pressed	Hitachi	311.4	497.4	20	3.21	
3. BN	hot pressed	ESK Kempten	250.3±0.5	665.1±1.2		2.08	
4. Graphite	POCO AXF-5Q	Union Oil Co.	245.8±1.0	674.0±6.0	19	1.80	
5. Graphite	EK 98	Ringsdorff	245.9±0.5	672.0±1.0	10	1.80	
6. Graphite	5890 PT	Carbone Lorraine	245.9±0.5	672.0±1.0	20	1.75	
7. Pyrolytic graphite		Carbone Lorraine	245.9	684.8		2.11	
8. α-SiC	α (4H+6H+15R)	ESK Kempten			1		
9. α-SiC	α (6H)+50%β+2%AlN	Hitachi			3	3.15	
10. α-SiC	α (4H+6H),+3%Al	ESK Kempten			1	3.20	
11. α-SiC	HIP, 0.1%Al	ESK Kempten				2.9	
12. α-SiC(+Si)	α (6H)+15%Si "Rocar"	Hoechst CeramTec					
13. β SiC	Si-impr.[1] EKA-50 graph.	KFA	345.9±0.1				18
14. β SiC	Si-impr. POCO graph.	KFA	345.9±0.1				13
15. β SiC	Si-impr. FE 49 graph.	KFA	345.9±0.1				13
16. Si_3N_4	80%α +20%β HP "Rosinit"	Hoechst CeramTec				2.27	
17. TiC	CVD coated POCO graphite	Ultramet Pacoima, CA	432.8				25
18. TiC	CVD coated Mo	Hitachi	432.5				12
19. TiC	CVD coated POCO graphite	Lab. Suisse Holog., Neuch.	432.7				25
20. TiN	CVD coated IN 625	Hitachi	425.4				15

[1] Liquid-Si impregnated followed by a reaction anneal at 1800°C to convert the adhering free Si to SiC.

thick test specimens were previously polished with 0.1µm diamond paste, ultrasonically cleaned in acetone and then alcohol, and well dried. All tests were made on specimens initially at room temperature. The tests were made by irradiating the same spot on each material for 5 times with normal ruby laser pulses. Additionally, Q-switched irradiation tests were made on SiC- and TiC-coated graphite specimens.

As a gauge for thermal spallation, the maximum depth of the ablation crater was measured under a microscope. These values were converted to an average spallation in g/cm^2 by multiplication by an estimated geometric factor and the bulk density.

4. RESULTS

The observed thermal damage mechanisms are classified as

1. local cracking (plastic flow at elevated temperatures followed by tensile stress cracking during cooling) (e.g. Fig. 8),
2. bending fracture (e.g. Fig. 3),
3. chemical decomposition (e.g. Fig. 6),
4. melting (e.g. Fig. 9), and
5. thermal spallation (e.g. Fig. 2).

Mechanical failure during heat up testing can, in principle, occur under any of the above named thermal stresses. In the present work, the testing procedure was terminated when the test area had received 5 pulse cycles. Therefore, fatigue effects due to accumulated yielding and creep, per se, were insignificant and not expected to be detectable. Thus, cracking is adopted in the present tests as the principal index for thermal stress failure. Ceramics generally have good compressive strength but relatively low tensile strength. Compressive fracture during heat up is unlikely. If ductile yielding or plastic flow occurs at elevated temperatures, however, then the test region will cool under tension[23,24,48]. During the cool down, then, ceramics may fail by tensile fracture. Bending thermal stresses are deemed able to induce fracture failure in ceramics either during heat up or cool down. All the fracture failures may be complicated by work hardening effects known to occur in some alloys or to brittle-to-ductile transformations.

Qualitative observations of the first four mechanisms are summarized in the order of decreasing $\Phi\sqrt{t_p}$ values (and decreasing power densities) in Columns 4, 7, and 10 of Table 4. The measured maximum depths of thermal spallation are listed in Columns 2, 5, and 8. Estimated average values of spallation loss in g/cm^2 are given in Columns 3, 6, and 9 of the same tables.

The materials listed in the order of increasing resistance to thermal spallation near the damage threshold are as follows:

- Si_3N_4
- BN
- TiN (coating)
- α-SiC
- AlN
- 5890 PT graphite
- EK 98 graphite
- POCO and pyrolytic graphite
- TiC (coatings on POCO or Mo) and β SiC (coatings on graphite).

5. DISCUSSION

The interaction of the laser test beam with the various ceramics is summarized as follows.

5.1 Si_3N_4

This material shows some chemical decomposition, thermal stress facturing, and a strong susceptibility to ablation by thermal spallation at the lowest power density tested.

Threshold values for Si_3N_4 thermal stress failure ("melting" probably due to decomposition, or "cracking") as reported by DeConich and Snykers[19] are $(\Phi\sqrt{t_p})_c = 2.0$ for 1 s and 0.82 $kJ/cm^2s^{1/2}$ for 0.1 s pulses. The present data, Table 2, give $(\Phi\sqrt{t_p})_c = 1.6$ for chemical decomposition and 0.8 $kJ/cm^2s^{1/2}$ for thermal fracturing and thermal spallation with 0.9 ms long pulses.

Table 4: Thermal stress damage of ceramics after different loading, $\Phi\sqrt{t_p}$, with five 900 µs long defocused normal laser pulses (1-20), and 5 µs long Q-switched laser pulses (21-22).

Material	$\Phi\sqrt{t_p}$ = 4.8 kJ/cm^{2}s$^{1/2}$ Defocus: 2 mm			$\Phi\sqrt{t_p}$ = 1.6 kJ/cm^{2}s$^{1/2}$ 3 mm			$\Phi\sqrt{t_p}$ = 0.8 kJ/cm^{2}s$^{1/2}$ 4 mm		
	depth* µm	loss mg/cm^2	other damage	depth µm	loss mg/cm^2	other damage	depth µm	loss mg/cm^2	other damage
1. AlN (ESK)	160	26	F+D	16	2.6	F+D	0	0	
2. AlN (Hi.)	150	24	F+D	17	2.7	F+D	0	0	
3. BN				85	8.8	D	35	3.6	D
4. POCO graphite	110	9.9	(R)	7	0.6	R	0	0	
5. EK 98 graphite	125	11	(R)	24	2.6	R	0	0	
6. 5890 PT graphite				35	3.9	R	4	0.4	
7. Pyrolytic graphite									
1.c direction	100	11	R+F+P	26	2.7	R+F+P	3	0.3	
2.a direction	36	3.8	F+P	3	0.3	F+P	0	0	
8. α-SiC (ESK)				48	7.7	F+Si melt	20	3.2	F+Si melt
9. α-SiC (Hi.)				45	7.2	F+Si melt+ vapn.	8	1.3	F+Si melt+ vapn.
10. α-SiC, 3 % Al				37	6.0	F(b)+Si melt	10	1.6	F(b)+Si melt
11. α-SiC, 0.1 % Al				21	3.6	F(b)+Si melt	0	0	F(b)+Si melt
12. α-SiC(+Si)				24	4.0	F+Si melt	0	0	F+Si melt
13. ß-SiC coated EKA-50				27	4.3	F+Si melt+ vapn.	0	0	F+Si melt
14. ß-SiC coated POCO	105	17	F+Si melt	< 4	< 0.6	F+Si melt	0	0	
15. ß-SiC coated FE 49	110	18	F+Si melt	4	0.6	F+Si melt	0	0	
16. Si_3N_4				100	20	D+F	83	10	D+F
17. TiC coated POCO	75	18	F+melt	12	3	F+melt	0	0	F
18. TiC coated Mo	14	3.5	F+melt	1	0.2	F+melt	0	0	
19. TiC on POCO				25	6	complete melting	25	6	complete melting
20. TiN on IN 625				50	12	flaking	16	4	flaking
	$\Phi\sqrt{t_p}$ = 8.8 kJ/cm^{2}s$^{1/2}$			$\Phi\sqrt{t_p}$ = 2.9 kJ/cm^{2}s$^{1/2}$			$\Phi\sqrt{t_p}$ = 1.5 kJ/cm^{2}s$^{1/2}$		
21. ß-SiC coated graphite	5	0.8	F+melt	2	0	F	0	0	
22. TiC coated POCO graphite	8	2.0	F+melt	0	0	F+melt	0	0	F+melt

* Maximum depth of the crater formed by thermal spallation and estimated by mean mass loss (mg/cm^2).

F Fracture or cracking; F(b) denotes fracturing rupture.

D Chemical decomposition with condensation of the metallic component.

R Surface restructuring in graphite.

P Peeling.

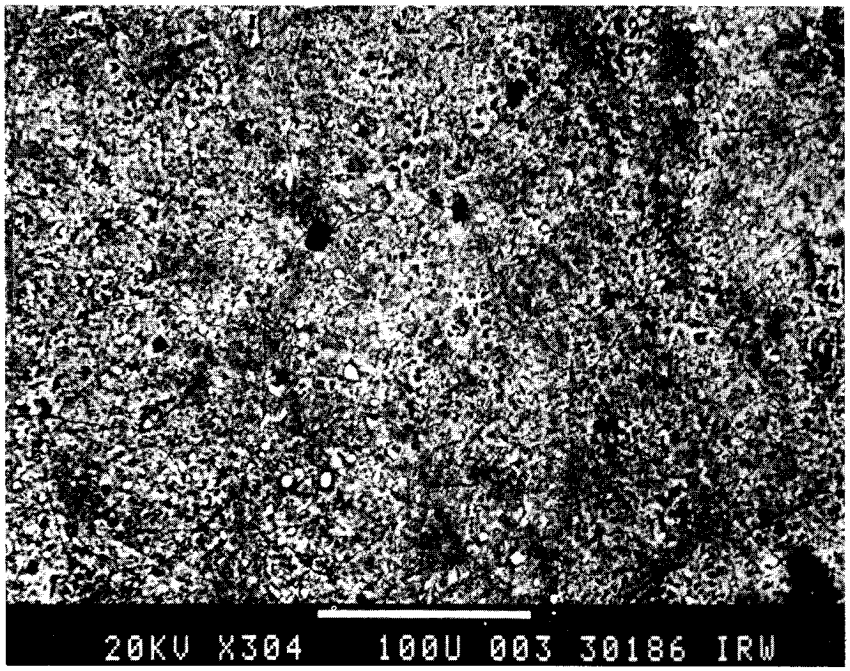

Fig. 2: SEM micrograph of Si_3N_4 after normal laser pulsing for 5 times at 4 mm defocus: $\Phi\sqrt{tp} = 0.8$ kJ/cm^{2}s$^{1/2}$.
The following modes of failure are seen:
a. thermal stress intergranular cracking (faintly visible),
b. chemical decomposition (the occasional bright sphere is free Si),
c. thermal spallation (only faintly visible relief).

The low resistance of the Si_3N_4 to thermal stress fracturing is surprising in view of the reported relatively low thermal expansion coefficient, ca. $2.5 \times 10^{-6} K^{-1}$, and Youngs's modulus, E = 90 GN/m^2 [22]. The intergranular fracturing seen in test areas, Fig. 2, suggest that the tested material may contain a sintering aid. Generally, Si_3N_4 material is regarded as having high potential but its process development is more deficient than other high temperature materials, e.g. the Young's modulus for a commerical body, 90 GN/m^2 [50], is considerably lower than that of a laboratory test specimen, 290 GN/^{2} [30]. Future work should include a study of the effect of the process parameters, porosity (and pore texture), sintering aid contents, proportion of the α, β and glassy modifications, hot pressing conditions, and grain size on the resulting thermal stress damage threshold $(\Phi\sqrt{tp})_c$. Eventually, characterization of the laser thermal stress induced microcracking on the strength of Si_3N_4 bodies could possibly lead to an improved understanding of Si_3N_4 as a engineering ceramic.

5.2 BN

As indicated in Columns 5 and 8 of Table 4, this material shows some chemical decomposition and a tendency for thermal spallation. These results are broadly in accord with the poor thermal shock resistance of BN in 5.5-kV electron beam tests as reported by DeConick and Snykers[19]. They differ from the 150-kV electron beam test results with 0.1 and 1 s pulse lengths as reported by Hoven et al.[36] who rate BN with the moderately good performing EK 98 graphite. A possible explanation for this discrepancy in that electron charge accumulated on the targets tested by Hoven et al. This effect could lead to an over estimate of the power density delivered by the 150 keV beam. DeConick and Snykers[19] explicitly designed their tests so as to eliminate this problem. The material investigated in this work had a density of only 92 % of the theoretical. Comparative tests with other grades, especially the pyrolytic form of BN, seem desirable for understanding the performance of this material.

5.3 CVD TiN-coated IN 625

Outer layers of this coating showed intergranular fracture and exfoliation at the lowest employed thermal stress parameter, $\Phi\sqrt{t_p} = 0.8$ kJ/cm^{2}s$^{1/2}$. Electron beam tests have been reported by Hoven et al.[36] to rapidly destroy the CVD TiN coating on Inconel by erosion and thermal shock. In contrast, Nakamura et al.[49] have reported that no failure occurs in a 20 µm thick CVD TiN coated IN 625 specimen irradiated with 30 keV protons under nearly the same thermal stress, $\Phi\sqrt{t_p} = 0.9$ kJ/cm^{2}s$^{1/2}$ and pulse length of $t_p = 0.2$ s. The latter good performance suggests a need for further work with the TiN coating process parameters.

5.4 Silicon carbides

The α-SiC test specimens, Items 8 to 12 in Table 4, show a strong tendency for tensile cracking (Fig. 3). The thermal fracture threshold is in all the listed materials below the lower limit of testing, $\Phi\sqrt{t_p} = 0.8$ kJ/cm^{2}s$^{1/2}$ for $t_p = 9\times10^{-4}$s. The two α-SiC Entries 10 and 11 of Table 4 show a strong sensivity to rupture by thermal shock bending.

An appreciable amount of melts in the form of tiny spheres appeared in the test areas of all the specimens (Fig. 4). Only the Item 12, α-SiC(+Si), contained free Si in the starting material. The observed melts in the tested areas of the Items 8 to 11 is assumed to have been produced by thermal de-

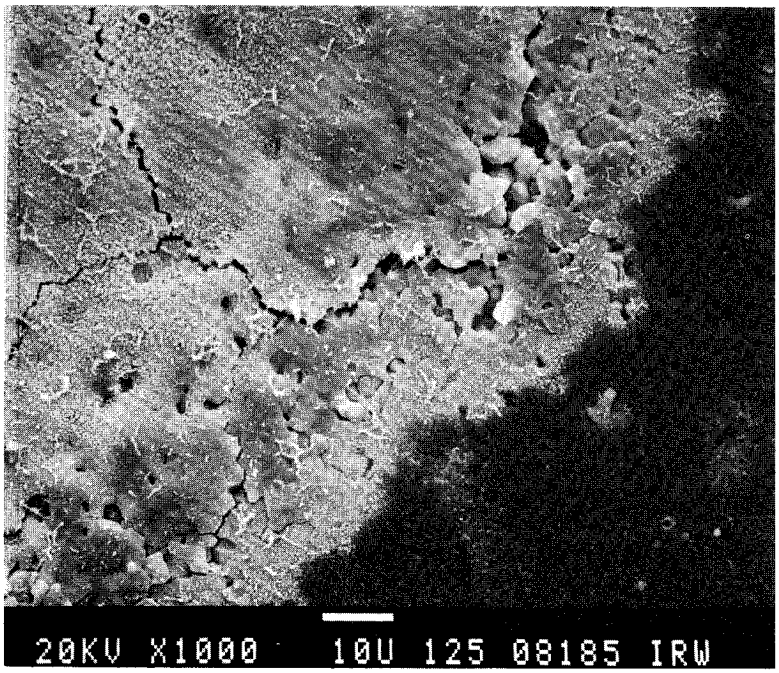

Fig. 3: SEM micrograph of Item 9. α -SiC (4H+6H)+3%Al (Hitachi) after pulsing for 5 times at 4 mm defocus: $\Phi\sqrt{tp} = 0.8$ kJ/cm^{2}s$^{1/2}$. Intergranular cracking in the test area is seen.

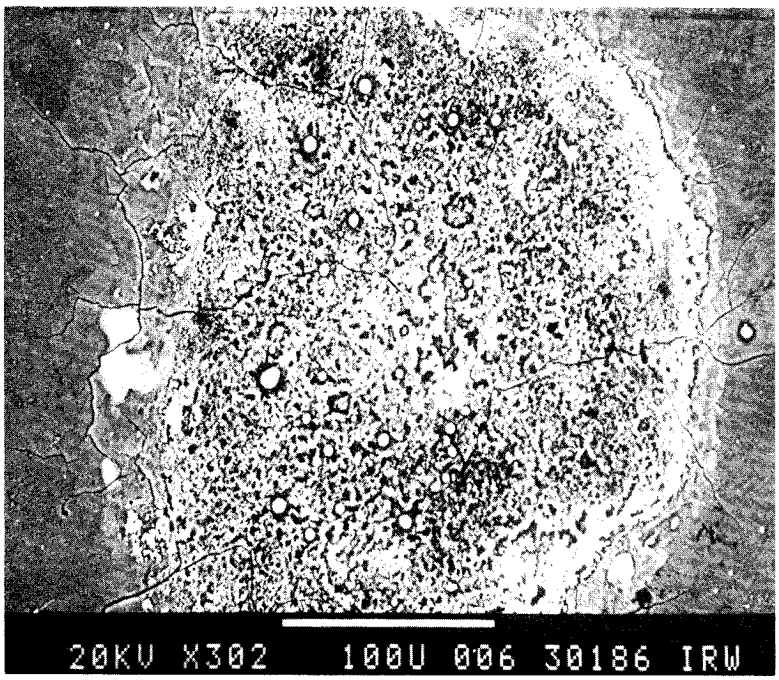

Fig. 4: SEM micrograph of Item 11. HIP α-SiC (ESK) after normal laser pulsing for 5 times at 4 mm defocus: $\Phi\sqrt{tp} = 0.8$ kJ/cm^{2}s$^{1/2}$. Melted spheres (white) and thermal stress cracking is seen. The intergranular cracks extend beyond the irradiated area.

composition of the AlN and melting of Al. Although SiC was earlier reported to decompose[31,54] this was later attributed to preferential vaporization of Si[56]. Now SiC is generally agreed to melt incongruently[35].

DeConinch and Snyders have reported results of 5.5 kV electron beam thermal shock tests on a commerical SiC materials of unspecified crystal form[19]. Values of the thermal stress failure ("melting and cracking") threshold parameter as calculated from their data as given in a plot generally decrease with decreasing pulse length from $\Phi\sqrt{tp} = 3.5$ for 1 s to 1.4 $kJ/cm^2s^{1/2}$ for 0.1 s pulses. The thermal stress cracking threshold of SiC of unknown crystal structure as measured with a 10 kV electron beam was reported by Ulrickson[67]. His data give $\Phi\sqrt{tp} = 1.8$ $kJ/cm^2s^{1/2}$ with a pulse length of 0.5 s. All the results are consistent in showing a monotone decrease in $\Phi\sqrt{tp}$ with decreasing pulse length.

A possible explanation for this unexpected result is that the more intense stress gradients generated with the shorter pulses act to enhance the rate of strain energy release. Also, energy losses by reflection of electrons (with the longer pulse lengths) is probably greater than the reflectivity losses with the electromagnetic radiation (shorter pulse length).

The α-SiC bulk materials examined appear to be unsuited as limiter or first wall materials for nuclear fusion devices with pulsed operation due to their low chemical stability and to the low thermal stress resistance. Poor thermal shock resistances in electron beam tests have also been reported by Hoven et al.[36].

Coatings of β-SiC on graphites performed better than the massive α-SiC modification ones described above in showing less tendency for thermal stress cracking. Two of the specimens with β-SiC coatings on AXF-5Q and EKA-50 graphite were tested with normal pulsing. Apart from the presence of free Si identified in the product test areas, both coatings survived the tests well and showed only a few difficultly detectable cracks at $\Phi\sqrt{tp} = 1.6$ $kJ/cm^2s^{1/2}$ (Fig. 5). The β-SiC coating on EKA-50 graphite shows fracturing and free Si in the tests but it is believed that these could have been due to free Si in the starting specimen.

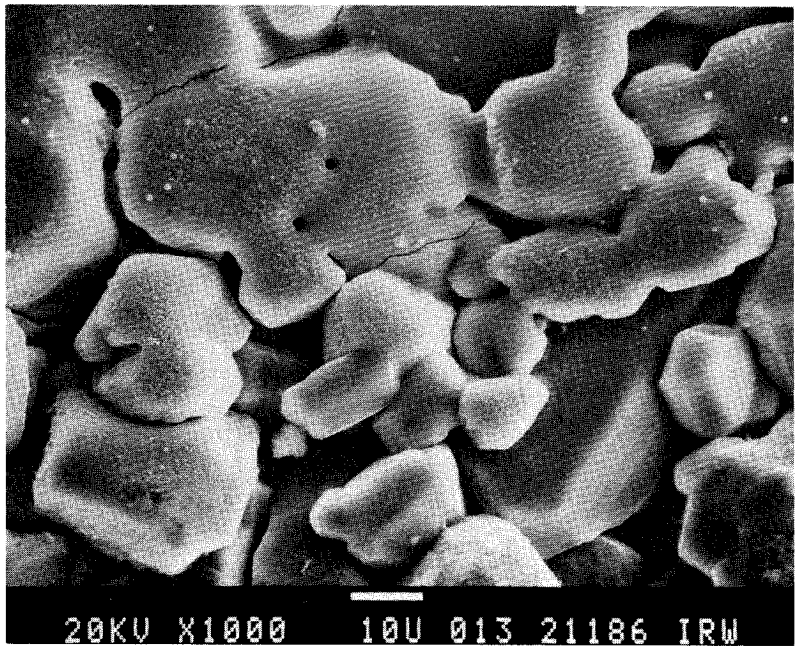

Fig. 5: SEM micrograph of β-SiC coated POCO graphite at the edge of the treated area after normal pulsing for 5 times at 3 mm defocus: $\Phi\sqrt{t_p} = 1.6$ kJ/cm^{2}s$^{1/2}$.
Inter- and intra-granular thermal stress fracturing is seen.

The third β-SiC coating on FE-49 graphite was subjected to Q-switched pulse tests. The product test area showed no detectable thermal stress cracking, but, did contain evidence of liquid stringers attributable to a superficial decomposition to a Si-rich liquid.

Thermal cracking threshold of β SiC coated POCO graphite lies between $\Phi\sqrt{t_p} = 0.8$ and 1.6 kJ/cm^{2}s$^{1/2}$ with $t_p = 9\times10^{-4}$s and near 0.8 kJ/cm^{2}s$^{1/2}$ with $t_p = 5\times10^{-6}$s. The thermal spallation threshold in β-SiC lies between $\Phi\sqrt{t_p} = 1.5$ and 2.9 kJ/cm^{2}s$^{1/2}$ with $t_p = 5\times10^{-6}$s. Further work should be done to better clarify the effects of thermal stressing on the fracture mechanics of β-SiC and to better define the conditions under which free Si does and does not form.

5.5 AlN

These materials show a strong susceptibility to thermal spallation at $\Phi\sqrt{tp} > 0.80$ kJ/cm^{2}s$^{1/2}$. The spallation is especially strong in the neighborhood of open pores. Chemical decomposition is evidenced by the appearance of condensed Al globules at $\Phi\sqrt{tp}$ = 1.6 kJ/cm^{2}s$^{1/2}$ (Fig. 6). Incipient fracturing occurs at $\Phi\sqrt{tp}$ = 4.8 kJ/cm^{2}s$^{1/2}$. These observations are qualitatively in agreement with the electron beam test results of Hoven et al.[36] who reported poor thermal shock resistance and fracturing behavior. Possibly the thermal shock performance could be improved by reducing the porosity, but, the chemical decomposition would be difficult to prohibit under the stated test conditions. Of all the nitrides, the AlN material shows the best stability toward thermal stressing and further work with $\Phi\sqrt{tp} \lesssim 0.8$ kJ/cm^{2}s$^{1/2}$ could be useful for optimizing process parameters.

5.6 Graphites

Some of these materials show good resistance toward thermal spallation. Measured depths of spallation are given in Columns 2, 5 and 8 of Table 4. Except for 5890 PT graphite with an undefined lower value, the thermal spallation threshould lie between $\Phi\sqrt{tp}$ = 0.8 and 1.6 kJ/cm^{2}s$^{1/2}$. The spallation craters show a rough surface characteristic of a microcrystalline detachment mechanism - any loss by sublimation and recondensation was not positively identified. The sublimation threshold for the reactor grade, ATJ, graphite has been measured with 10-kV electrons by Ulrickson[67] for which $\Phi\sqrt{tp}$ = 3.5 and calculated by Behrisch[8] from theoretical considerations as 3.7 kJ/cm^{2}s$^{1/2}$.

Pyrolytic graphite with beam impingement normal to the layer planes and all the other graphites show a surface restructuring at $\Phi\sqrt{tp}$ = 1.6 kJ/cm^{2}s$^{1/2}$. This restructuring can, also, be observed with higher power densities; but, then only in the test area fringes where the spallation is negligible. The pattern is very similar to that reported for proton beam irradiation by Sone et al.[60] as illustrated in their Fig. 6. The size of the structural features, 0.2 μm, is comparable to the ridge widths in a different (modified) surface restructuring pattern was reported by Saidoh et al.[55] and Das et al.[21]. A different surface pattern is seen in pyrolytic graphite irradiated parallel to the layer planes, Fig. 7.

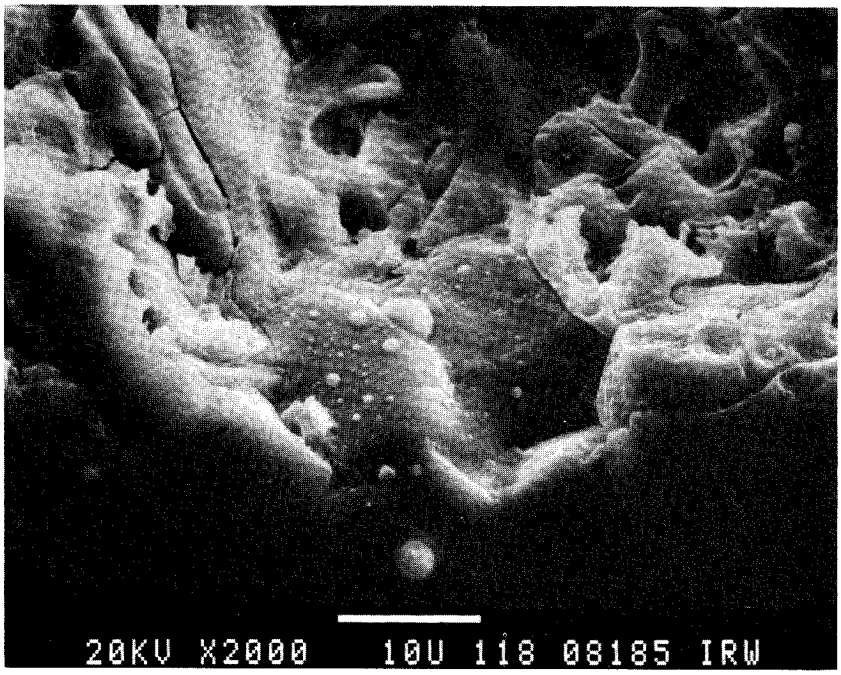

Fig. 6: SEM micrograph of AlN after being irradiated with one normal pulse at 3 mm defocus: $\Phi\sqrt{t_p} = 1.6$ kJ/cm^{2}s$^{1/2}$.
The rim of an erosion crater is seen. Thermostress cracks and condensed Al globules (product of AlN thermal decomposition) are present.

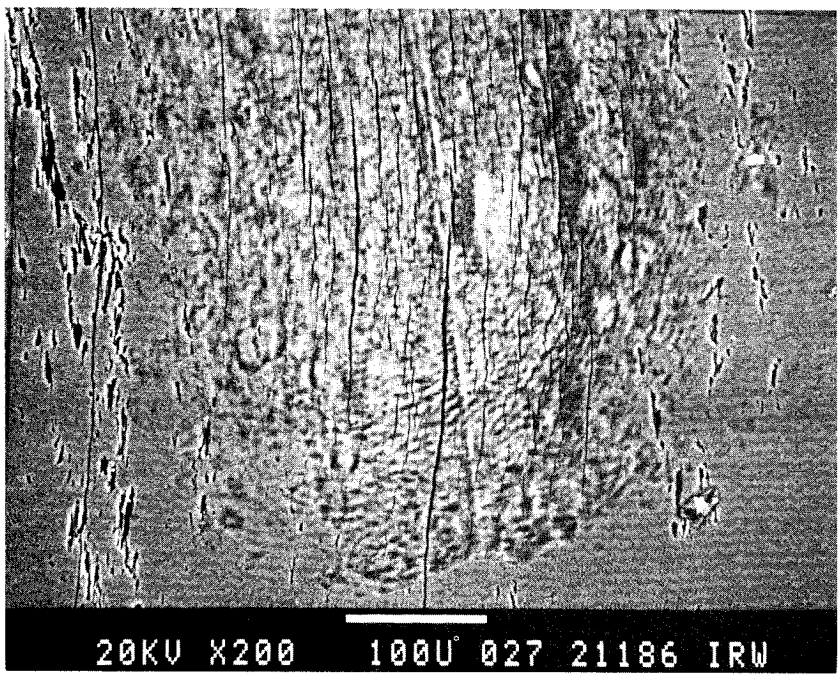

Fig. 7: SEM micrograph of pyrolytic graphite viewed parallel to the layer planes running vertically after pulsing for 5 times with normal laser radiation at 2 mm defocus: $\Phi\sqrt{t_p} = 4.8$ kJ/cm^{2}s$^{1/2}$.
Thermal stress splitting of the layer planes in the test area (upper central part of the picture) is seen. Surface restructuring with periodicities of ~ 10 µm is seen. This is much coarser than the restructuring feature sizes of 0.2 µm seen in layer planes irradiated normally (cf. Fig. 6 of Sone et al.[60]).

The extent of thermal spallation of pyrolytic graphite when the beam impinges normal to the layer planes is different from that when it impinges parallel. From the data seen in Table 4, the spallation threshould must lie just under $\Phi\sqrt{tp} = 0.8$ for perpendicular and just below 1.6 $kJ/cm^2s^{1/2}$ for parallel incidence to the layer planes. Ulrickson has reported sublimation thresholds for 10 kV electron beam bombardment according to which $\Phi\sqrt{tp} = 1.3$ for perpendicular and 11 $kJ/cm^2s^{1/2}$ for parallel incidence to the layer planes[67].

Rather pronounced thermal stress fracturing in graphites by pulsed 150 kV electron beam irradiation testing has been reported by Hoven et al.[36]. Such cracking was not observed in the present laser beam test results.

5.7 CVD TiC-coated AXF-5Q graphite

A fine-grained CVD TiC coated POCO graphite specimen supplied by the Neuchatel Lab. in Switzerland behaved unsatisfactorily in showing strong absorption of radiation and complete melting at the lowest normal test power density.

All the other specimens with larger grain size CVD TiC coatings, 25 µm on graphite and 12µm on Mo, rank with pyrolytic graphite and ß SiC coatings in showing good resistance toward ablation in normal radiation tests. Spallation thresholds lie between $\Phi\sqrt{tp} = 0.8$ and 1.6 $kJ/cm^2s^{1/2}$. However, melting and thermal stress cracking (Fig. 8) may occur in coatings on graphite even at the lowest power densities of tests, 26 kW/cm^2 (normal pulse, $\Phi\sqrt{tp} = 0.8$ $kJ/cm^2s^{1/2}$) and 250 kW/cm^2 (Q switch pulse, $\Phi\sqrt{tp} = 0.56$ $kJ/cm^2s^{1/2}$). The crack pattern, seen in Fig. 9, is very similar to that reported earlier by Bastow and Coworkers[7]. Outer layers of the TiC coatings sometimes tend to peel concave outwards and sometimes exfoliate. The microcracking threshold from the present results is $\Phi\sqrt{tp} = 0.56$ $kJ/cm^2s^{1/2}$. Mullendore et al.[47] have reported thermal fatigue measurements on TiC coated graphite irradiated with 30 kV electrons for which $\Phi\sqrt{tp} = 2.45$ $kJ/cm^2s^{1/2}$ and reported no damage, but, Mattox et al.[46] describe the presence of microcracks. Ulrickson[67] has reported data on the cracking threshold to TiC coated graphite at $\Phi\sqrt{tp} = 2.3$ $kJ/cm^2s^{1/2}$ based on 10-kV electron beam irradiation tests. Microcracking and upheaval of 7µm thick TiC coatings on POCO graphite have been reported to occur when cycled 1000 times with an

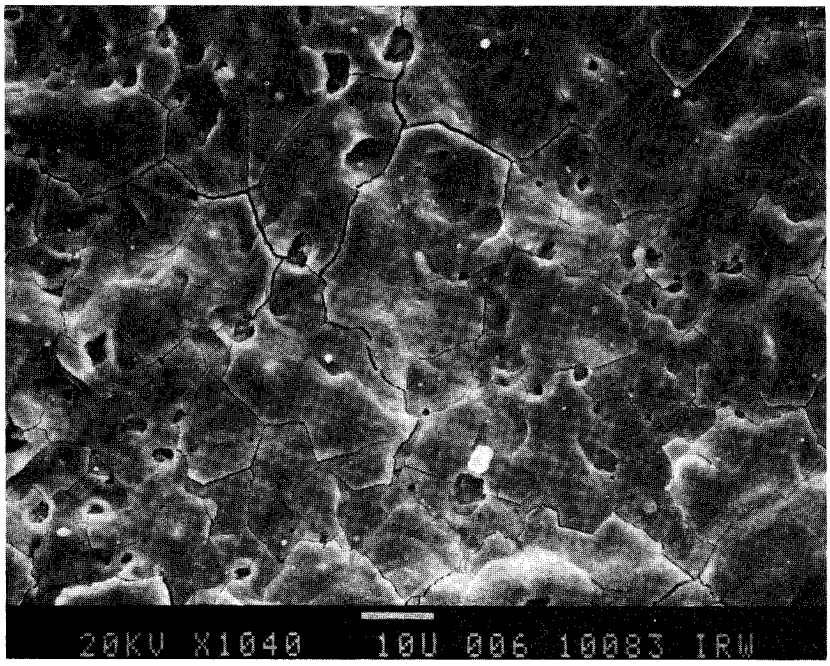

Fig. 8: SEM micrograph of CVD TiC-coated AXF-5Q graphite after Q-switch laser pulsing for 5 times at 2 mm defocus: $\Phi\sqrt{t_p}$ = 0.8 kJ/cm^{2}s$^{1/2}$. Melting of TiC followed by intergranular thermal-stress fracturing during cool down is seen. The fracture patterns is the same as that observed with massive TiC grown by diffusion reaction and subjected to the same test. This shows that the cracking is an inherent characteristic of TiC and not derived from differential thermal expansion between the coating and substrate.

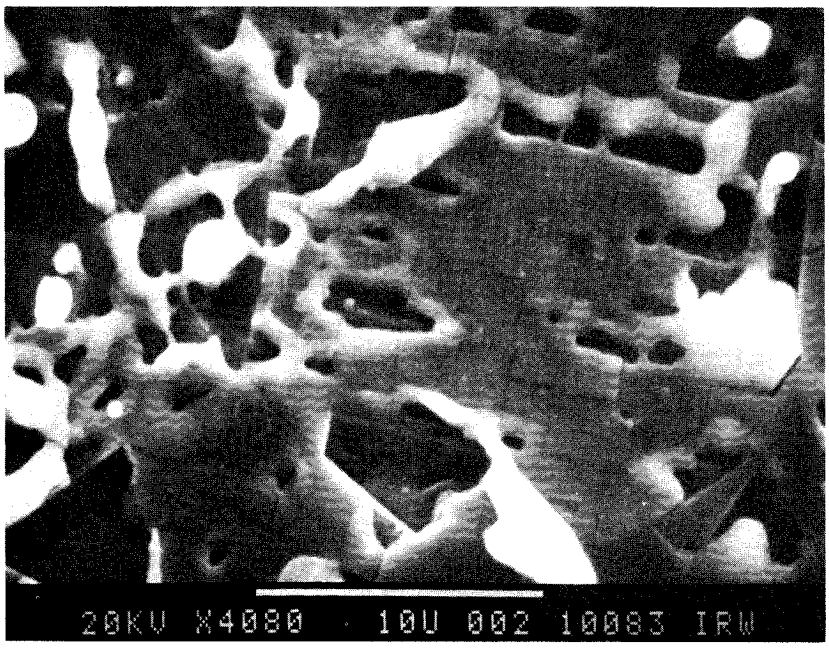

Fig. 9: SEM micrograph of CVD TiC coated AXF-5Q graphite after Q-switch laser pulsing for 30 times at 6 mm defocus: $\Phi\sqrt{t_p}$ = 0.56 kJ/cm^{2}s$^{1/2}$. Thermal stress cracking and evidence of fusion is seen. Outer layers of some of the coating have peeled away from the underlying TiC. Nakamura et al.[49] have previously reported a similar tendency to delaminate in CVD TiC coatings under H^+ bombardment with $\Phi\sqrt{t_p}$ = 1.5 kJ/cm^{2}s$^{1/2}$.

infrared image lamp between 500 and 1200°C but not when cycled between 500 and 1100°C[74]. Sevier et al.[57] have reported data in plot from which the TiC coating on POCO graphite has a melting threshold of $\Phi\sqrt{t_p}$ = 11.3 with 0.5 s and 8.0 kJ/cm^{2}s$^{1/2}$ with 1s and a microcracking threshold of $\Phi\sqrt{t_p}$ = 1.34 with 0.05 s and 0.92 kJ/cm^{2}s$^{1/2}$ with 1-s pulses.

Q-switched laser tests were made on CVD TiC-coated FE 49 graphite. The performance was good but inferior to that of the β-SiC coatings because thermal stress microcracking occurs in TiC but not in β-SiC under Q-switched radiation with $\Phi\sqrt{t_p}$ = 0.6 to 1.5 kJ/cm^{2}s$^{1/2}$ (defocus 2 to 6 mm).

Future tests on CVD TiC-coated graphite are planned to clarify the dependence of the damage threshold $\Phi\sqrt{t_p}$ on pulse length, power density, and target temperature, the brittle-to-ductile transition temperature and to ascertain when the microcracks can heal and when they can lead to deterioration.

5.8 CVD TiC-coated Mo

This coating shows the greated resistance to thermal spallation of all the test specimens subjected to the laser beam tests. Grain boundary cracking appears at $\Phi\sqrt{t_p}$ = 1.6 kJ/cm^{2}s$^{1/2}$ but no cumulative or fatigue effects was detected in the 5-cycle test procedure. The observed intergranular cracking (Fig. 10) is associated with a reaction of the TiC with Mo and formation of a low melting Mo-TiC eutectic[39]. Nakamura et al.[49] have reported that a 20-μm thick TiC coating on Mo does not exfoliate at the threshold for substrate melting, $\Phi\sqrt{t_p}$ = 1.18 kJ/cm^{2}s$^{1/2}$, when tested in a 30 keV beam of protons with t_p = 0.35 s.

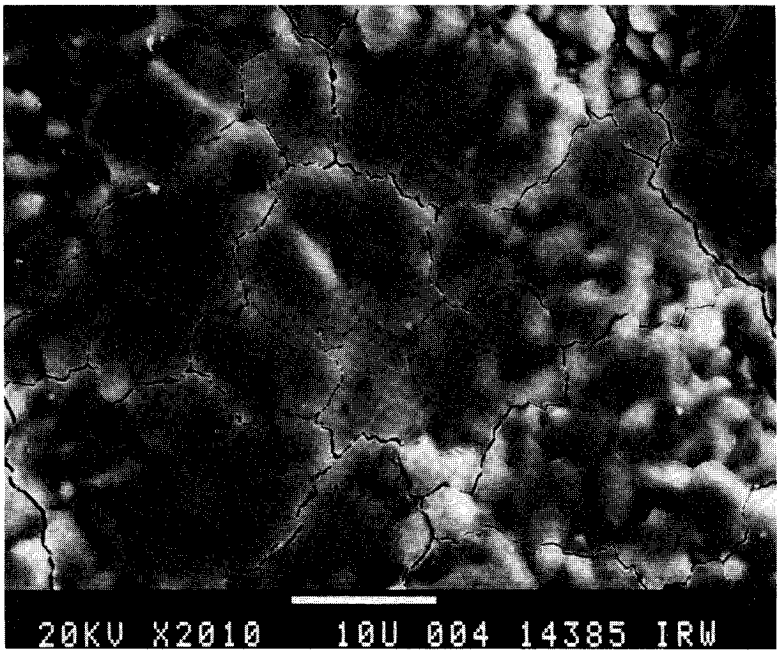

Fig. 10: SEM micrograph of CVD TiC coated Mo after normal laser pulsing for 5 times at 3 mm defocus: $\Phi\sqrt{tp}$ = 1.6 kJ/cm^{2}s$^{1/2}$.
Partial melting and intergranular cracking is apparent. TiC lowers the melting point of Mo due to eutectic formation[25].

6. CONCLUSIONS

The quantity $\Phi\sqrt{tp}$ has been shown to be useful for comparing and correlating beam irradiation test results on ceramics from different laboratories for a wide range of pulse lengths, and for different kinds of beams (proton, electron, and electromagnetic).

A secondary aim of this work was to identify qualitatively fracture mechanisms and the kind of associated thermal stresses in the materials. Such information can be helpful as a guide in optimizing process parameters and the materials performance under service conditions.

This work was concentrated on only a few selected qualities of materials. There is a need to extend the technique to test other grades of materials in order to better characterize that grade with optimum resistance to thermal stressing.

7. ACKNOWLEDGEMENTS

The β-SiC coated graphite specimens were supplied by Dr. E. Gyarmati of this laboratory. Metallography was done by Messrs. H. Hoven, W.J. Frings, and Mrs. R. Fisseler. The scanning electron microscopy was done by Dr. E. Wallura and Mr. F. Els. The laser shots were made by Mr. U. Schwalm and Mrs. Dr. M. Mazurkiewicz.

8. REFERENCES

1. M. von Allmen: J. Appl. Phys. 47 (1976) 5460-3

2. M. von Allmen: "Coupling of Beam Energy to Solids", in Laser and Electron Beam Processing in Materials, C.W. White and P.S. Peercy (eds.), Acad. Press, 1980, pp. 6-19

3. M. von Allmen, P. Blaser, K. Affolter, and E. Stürmer: IEEE J. Quantum Electronics, QE-14 (1978) 85-88

4. N.J. Archer: "The Preparation and Properties of Pyrolytic Boron Nitride in High Temperature Chemistry of Inorganic and Ceramic Materials", F.P. Glasser and P.E. Potter (eds.), The Chemical Society, Burlington House, London 1976, 167-179

5. P. Baeri, S.U. Carnpisano, G. Foti, and E. Rimini: J. Appl. Phys. 50 (1979) 788-797

6. N.G. Basov, V.A. Boiko, O.N. Krokhin, O.G. Semenov, and G.V. Sklizkow: Sov. Phys.-Tech. Phys. 13 (1969) 1581-2

7. T.J. Bastow, M.E. Packer, and N. Gane: Nature 222 (1969) 27-9

8. R. Behrisch: J. Nucl. Mater. 93+94 (1980) 498-504

9. H.E. Bishop: "Electron-Solid Interactions and Energy Dissipation", in Quantitative Scanning Electron Microscopy, D.B. Holt, M.D. Muir, P.R. Grant, and I.M. Boswarva (eds.), Acad. Press, 1974, pp. 41-64

10. L.M. Blinov, E.A. Bobrova, V.S. Vavilov, and G.N. Galkin: Sov. Phys.-Solid State, 9 (1968) 2537-42

11. L.M. Blinov, V.S. Vavilov, and G.N. Galkin: Sov. Phys.-Solid State 9 (1967) 666-669

12. E.A. Bobrova, V.S. Vavilov, and G.N. Galkin: Sov. Phys.-Solid State 12 (1970) 959-961

13. A.M. Bonch-Bruevich, Ya.A. Imas, G.S. Romanov, M.N. Libenson, and L.N. Mal'tsev: Sov. Phys.-Tech. Phys. 13 (1968) 640-643

14. E.P. Butler: Mater. Sci. Technol. 1 (1985) 417-432

15. H.S. Carslaw and J.C. Jaeger: "Conduction of Heat in Solids", Oxford Press, 2nd ed., 1959, p. 78-80

16. A.H. Clauer, J.H. Holbrook, and B.P. Fairand: "Effects of Laser Induced Shock Waves on Metals", in Shock Waves and High-strain-rate Phenomena in Metals, M.A. Meyers and L.E. Murr (eds.), Plenum Press, 1981, p. 675-702

17. W.K. Chun and K. Rose: J. Appl. Phys. 41 (1970) 614

18. R.L. Coble and W.D. Kingery: J. Am. Ceram. Soc. 38 (1955) 33-37

19. R. de Coninck and M. Snykers: J. Nucl. Mater. 76+77 (1978) 629-633

20. W.B. Crandall and J. Ging: J. Am. Ceram. Soc. 53 (1955) 44-54

21. S.K. Das, M. Kaminsky, R. Tishler, and J. Ceochi: J. Nucl. Mater. 85+86 (1979) 225-230; see also ibid Thin Solid Films 63 (1979) 227-236

22. R.W. Davidge and G. Tappin: Brit. Ceram. Soc. 66 (1967) 405-412

23. R.W. Davidge and G. Tappin: J. Mater. Sci. 3 (1968) 164-73

24. R.A. Dugdale: "Thermal Shock and Thermal Stress Fatigue in a Stabilised Pinch Fusion Reactor", R.A. Dugdale, A.E.R.E.-R 2955, 1959

25. R.A. Dugdale, R.C. McVickers, and S.D. Ford: J. Nucl. Mater. 12 (1964) 1-15

26. W.P. Dumke: Phys. Lett. 78A (1980) 477-80

27. V.N. Eremenko and T.Ya. Velikanova: Sov. Powder Met. and Metal Ceram. No. 5(17) (1963) 347-352

28. A.G. Evans and R.W. Davidge: J. Mater. Sci. 5 (1970) 314-325

29. B.P. Fairand and A.H. Clauer: "Laser Generated Stress Waves: Their Characteristics and Their Effects of Materials", in Laser-Solid Interactions and Laser Processing 1978, S.D. Ferris, H.J. Leamy, and J.M. Poate (eds.), Am. Inst. Phys., 1979, pp. 27

30. W.A. Fate: J. Appl. Phys. 46 (1975) 2375-7

31. E. Friederich and L. Sittig: Z. Anorg. Allgem. Chem. 144 (1925) 169-89

32. G.N. Galkin, L.M. Blinov, et al.: JETP Lett. 7 (1969) 69

33. J.-C. Glandus and P. Boch: "Elastic and Anelastic Properties of Nitrogen Ceramics", in Nitrogen Ceramics, F.L. Riley (ed.), Alphen aan den Rijn: Sijthoff Noordhoff Pub., 1977, pp. 515-9

34. E. Glenny: Metallurgical Revs. 6 (1961) 387-465

35. M. Hansen and K. Anderko: Constitution of Binary Alloys, McGraw-Hill, 1958

36. H. Hoven, K. Koizlik, J. Linke, H. Nickel, and E. Wallura: "Materials for High Heat Flux Components of the First Wall in Fusion Reactors", Jül-2002 (Aug. 1985)

37. M.I. Kaganov, I.M. Lifshitz, and L.V. Tanatarov: Soc. Phys. JETP 4 (1957) 173-178

38. W.D. Kingery: J. Am. Ceram. Soc. 38 (1955) 3-15

39. A. Kohyama and N. Igata: J. Nucl. Mater. 103+104 (1981) 415-420

40. F.F. Lange: J. Am. Ceram. Soc. 56 (1973) 445

41. J.M. Liu, R. Yen, H. Kurz, and N. Bloembergen: Appl. Phys. Lett 39 (1981) 755-57

42. J.M. Liu, H. Kurz, and N. Bloembergen: Appl. Phys. Lett. 41 (1982) 643-646

43. D.E. Lloyd: "High-Temperature Properties of Reaction-Sintered and Hot-pressed Si_3N_4", Special Ceramics, v. 4, P. Popper (ed.), Brit. Ceram. Soc., (1968), pp. 165-172

44. G.M. McCracken and P.E. Stott: Nucl. Fusion 19 (1979) 889-981

45. F. Mast and H. Vernickel: J. Nucl. Mater. 111+112 (1982) 566-568

46. D.M. Mattox, A.W. Mullendore, J.B. Whitley, and H.O. Pierson: Thin Solid Films 73 (1980) 101-107

47. A.W. Mullendore, J.B. Whitley, and D.M. Mattox: J. Nucl. mater. 93+94 (1980) 486-492

48. H.M. Musal, Jr.: "Thermochemical Stress Degradation of Metal Mirror Surfaces Under Pulsed Laser Irradiation", NBS Spec. Pub. 568 (1980), pp. 159-173

49. K. Nakamura, R. Yamada, M. Saidoh, and Y. Murakami: J. Nucl. Mater. 111+112 (1982) 852-855

50. H.J. Pohlmann, H.R. Maier, and A. Krauth: "Recuperative Ceramic Heat Exchanger Gas Turbine Application", in The Mechanical Engineering Properties and Applications of Ceramics, D.J. Godfrey (ed.), Proc. Brit. Ceram. Soc., Stoke-on-Trent, No. 26, 1978, pp. 31

51. R.J. Price: Nucl. Technol. 35 (1977) 320-336

52. J.F. Ready: J. Appl. Phys. 36 (1965) 462

53. J.F. Ready: "Effects of High-Power Laser Radiation", Academic Press, 1971, Chapter 3

54. O. Ruff and M. Konschak: 32 (1926) 515-25

55. M. Saidoh, R. Yamada, and K. Nakamura: J. Nucl. Mater. 102 (1981) 97-108

56. R.I. Scace and G.A. Slack: "The Si-C and Ge-C Diagrams", in Silicon Carbide A High Temperature Semiconductor, J.R. O'Connor and J. Smiltens (eds.), Pergamon Press, 1960, pp. 24-28

57. D.L. Sevier, P.W. Trester, G. Hopkins, T.E. McKelvey, and T.S. Taylor: J. Nucl. Mater. 103+104 (1981) 187-192

58. P.T.B. Shaffer: Materials Index, No. 1, Plenum Press, 1964

59. C.J. Smithells: Metals Reference Book, V. III, Butterworths, 1967, 4th ed.

60. K. Sone and M. Saidoh et al.: J. Nucl. Mater. 98 (1981) 270-278

61. Stopping Powers for Electrons and Positrons, ICRU Rept. 37, Intern. Comm. Rad. Units and Measurements, 7910 Woodmont Ave., Bethesda, MD, 20814, USA, 1984

62. H. Tanaka, K. Saiki, S. Otani, A. Koma and S. Tanaka: J. Nucl. Mater. 116 (1983) 317-320

63. S. Timoshenko and J.N. Goddier: Theory of Elasticity, McGraw-Hill, 1951.

64. Y.S. Touloukian (ed.): "Thermophysical Properties of High Temperature Solid Materials", V. 1, 2, 4, and 5, MacMillan Co. 1967

65. Y.S. Touloukian and E.H. Buyko: "Thermophysical Properties of Matter, Specific Heat", V. 4 and 5, Plenum 1970

66. Y.S. Touloukian, R.W. Powell, C.Y. Ho, and P.G. Klemens: "Thermalphysical Properties of Matter", V. 1 and 2, Thermal Conductivity, Plenum, 1970

67. M. Ulrickson: J. Nucl. Mater. 85+86 (1979) 231-235

68. J.H. Weaver, C. Krafka, D.W. Lynch, and E.E. Koch: Physics Data, Pt. I and II, Optical Properties of Metals, H. Behrens and E. EBEL, Fachinformationszentrum Energie, Physik, Mathematik GmbH, Karlsruhe, 1981

69. R.M. White: J. Appl. Phys. 34 (1963) 3559-3567

70. M.W. Williams and E.T. Arakawa: J. Appl. Phys. 43 (1972) 3460-3

71. J.P. Woerdman: Philips Res. Repts. Suppl. 26 (1971) 1-81

72. E.J. Yoffa: Phys. Rev. B21 (1980a) 2415

73. E.J. Yoffa: Appl. Phys. Lett. 36 (1980b) 37-8

74. S. Yamanaka, H. Ohara, P. Son, and M. Miyake: J. Nucl. Mater. 122+123 (1984) 1304-8

75. T.A. Zaker: J. Appl. Mech. 32 (1965) 143-150